

A Nonlinear Method to Estimate Source Parameters, Amplitude, and Travel Times of Teleseismic Body Waves

by R. F. Garcia,* L. Schardong,* and S. Chevrot*

Abstract We present a nonlinear waveform inversion method to determine source parameters under point-source approximation (depth, source time function, centroid moment tensor, and seismic moment) and also travel times and amplitudes of body waves from teleseismic records. We demonstrate that our source time function estimates significantly improve correlation between observed and synthetic broadband seismograms. The scaling of source dimensions with seismic moment is similar for deep and shallow events in the Japanese subduction area for moment magnitudes between 6.1 and 7.5. We compare event depths and moment tensors obtained with our method to those reported by different institutions for a set of Japanese earthquakes. This comparison reveals that our method gives hypocentral depths closer to those obtained with regional arrays than other teleseismic methods. The seismic moment is properly recovered, but data weighting strongly influences the moment tensor solution. Focal mechanisms are biased by high-frequency body-wave amplitude variations due to crustal structure below the stations and by errors on the instrument responses. Body-wave differential travel times are improved compared with phase-picking measurements. The high-quality travel times will be exploited to obtain more precise event locations and higher resolution tomographic models.

Online Material: Coordinates of Japanese earthquakes processed in this study.

Introduction

Modern digital seismological records are routinely exploited to constrain the seismic sources and Earth structure. The first studies relied on long-period records of surface and body waves to determine source parameters (Dziewonski *et al.*, 1981; Sipkin, 1982; Dziewonski, Chou, and Woodhouse, 1983; Sipkin, 1994). However, even at long periods, there is a trade-off between the hypocentral depth and some components of the moment tensor, and the amplitudes of body waves show large variations around their expected values (Ruff, 1989). Moreover, the source duration is estimated through an empirical scaling to seismic moment (Dziewonski *et al.*, 1981). Many event location procedures still rely on travel-time picks that can be affected by large reading errors and biases (Röhm *et al.*, 1999). Improvements in relocation algorithms applied to travel-time picks collected by the International Seismological Center (ISC) (Engdahl *et al.*, 1998) have recently been implemented at the ISC (Bondár and McLaughlin, 2009; Bondár and Storchak, 2011), but the location errors are still significant. There is a need for higher quality travel-time data sets obtained by waveform

fits to improve the location of teleseismic events. Global and regional tomographic studies would also benefit from such a data set.

In this paper, an automatic nonlinear algorithm for the analysis of broadband records of teleseismic body waves is designed to improve the recovery of source parameters and travel times. In particular, broadband estimates of source time functions and event depth are important to compute reliable synthetic seismograms and measure travel time and amplitude perturbations with cross-correlation methods, which are the basic ingredients of finite-frequency tomography.

Waveform Modeling

The displacement associated with a teleseismic body wave produced by a point source is given by

$$\mathbf{W}(t) = \dot{M}(t) * : \nabla G(t), \quad (1)$$

where $*$ denotes the convolution product, $:$ the tensor product, ∇ the gradient along source coordinates, $\mathbf{W}(t)$ the displacement vector, $M(t)$ the moment tensor function, and $G(t)$ the Green's tensor. Under the point-source approximation, the moment tensor function is given by

*Also at CNRS; IRAP; 14, avenue Edouard Belin, F-31400 Toulouse, France.

$$\dot{M}(t) = M_0 S(t) \mathbf{M}, \quad (2)$$

where M_0 is the seismic moment, \mathbf{M} is the normalized moment tensor, and $S(t)$ is the source time function (STF), or moment rate function, of the earthquake. This function is normalized in such a way that its time integral equals unity. Using asymptotic far-field ray theoretical Green's functions, the component n of surface displacement at station i can be written as

$$W_i^n(t) = \sum_{j=1}^{N_i} M_0 R_{ij} A_{ij}^G S(t) * \delta(t - t_{ij}) * Att(t_{ij}^*, t) p_{ij}^n, \quad (3)$$

where N_i is the number of body waves arriving at station i ; $R_{ij} = \mathbf{p}_{ij} \cdot \mathbf{M} \cdot \mathbf{e}_{ij}$ is the radiation pattern of body-wave j arriving at station i depending on unit vectors \mathbf{e}_{ij} and \mathbf{p}_{ij} that describe, respectively, the ray direction at the source and the body-wave polarization at the receiver; A_{ij}^G , t_{ij} , and t_{ij}^* are, respectively, the ray theoretical amplitude, travel time, and attenuation parameters of body-wave j recorded at station i . $\delta(t)$ is the Dirac delta function. $Att(t^*, t)$ is the inverse Fourier transform of the attenuation operator defined by $Att(t^*, f) = \exp(-\pi f t^*) \exp[-2if \ln(\frac{f}{f_0} t^*)]$, with the reference frequency f_0 (Červený, 2001). The quality factor and t^* do not depend on frequency in this formulation. The ray theoretical amplitude A_{ij}^G includes geometrical spreading and the reflexion/transmission coefficients for all the model interfaces, including the free surface at the receiver. A_{ij}^G and t_{ij} are calculated using outputs of the tau-p algorithm (Buland and Chapman, 1983) using the “ttimes” software.

To simplify the notation, the body-wave displacement vector $\mathbf{W}_{ij}(t)$ is assumed to be projected on the vertical, radial, or transverse components, respectively, for body waves arriving at the station as P , SV , or SH waves. With this notation, $W_{ij}(t) = W_{ij}^n(t)$. Now assuming $A_{ij} = R_{ij} A_{ij}^G p_{ij}^n$, the surface displacement due to a single body-wave arrival j at station i (implicitly along corresponding component n) is

$$W_{ij}(t) = M_0 A_{ij} S(t) * \delta(t - t_{ij}) * Att(t_{ij}^*, t). \quad (4)$$

Waveform Inversion

The recovery of the model parameters by the waveform fit is a highly nonlinear problem. The source and body-wave parameters, as well as their trade-off, are described in the following section. Data selection and normalization, the nonlinear inversion method, two different inversion strategies, and limitations of the method are described later.

Model Parameters

Intrinsic trade-offs are evident between source parameters and body-wave travel times, amplitudes, and waveforms.

The first trade-off is between the body-wave travel times (t_{ij}) and the source location. This is well-known because the earthquakes are usually located using body-wave travel

times. To remove this trade-off, the latitude, longitude, and origin times of hypocenters are fixed and extracted from the Engdahl-Van der Hilst-Buland (EHB) catalog (Engdahl *et al.*, 1998), and ISC relocations after 2009 (Bondár and McLaughlin, 2009). By doing so, the effect of errors on these parameters is implicitly included in the body-wave travel times (t_{ij}). However, we refine the hypocentral depth (d_q) by exploiting the differential travel times between direct and depth phases, as described next.

The second intrinsic trade-off is between the seismic moment (M_0), the normalized centroid moment tensor (\mathbf{M}), the source time function [$S(t)$], the amplitude (A_{ij}), and attenuation (t_{ij}^*) parameters of the body waves. We infer this trade-off by presenting the results of two inversion strategies in the [Inversion Strategies](#) section. The initial moment tensor (M_0 and \mathbf{M}) is taken from the Global CMT project. The normalized moment tensor (\mathbf{M}) is imposed to be a pure double couple. The initial source time function [$S(t)$] is the absolute value of a stack of P waveforms. A positivity constraint is imposed to the source time function during the inversion.

The values of amplitudes and travel times for each phase and for a set of source parameter values (M_0 , \mathbf{M} , $S(t)$, and d_q) are computed from the ak135 Earth model (Kennett *et al.*, 1995) and are noted with a superscript o . The dependence of body-wave amplitude (A_{ij}^o) and travel-time (t_{ij}^o) values on source parameters is not explicitly written for clarity, but it is the base of the trade-off between source and body-wave parameters.

In addition to the previously described source parameters (M_0 , \mathbf{M} , $S(t)$, and d_q), we invert for perturbations of amplitudes (δA_{ij}), travel times (δt_{ij}), and attenuation (t_{ij}^*) of direct body waves, and amplitude perturbations of their depth phases (δA_{ij}^p and δA_{ij}^s). The differential travel times between direct and depth phases, $\Delta t_{ij}^p(d_q)$ and $\Delta t_{ij}^s(d_q)$, are fixed by the event depth (d_q). Consequently, each body-wave record is described by

$$\begin{aligned} W_{ij}(t) + W_{ij}^p(t) + W_{ij}^s(t) \\ = M_0 S(t) * Att(t_{ij}^*, t) * A_{ij}^o \delta A_{ij} \{ \delta(t - t_{ij}^o - \delta t_{ij}) \\ + \frac{A_{ij}^{po}}{A_{ij}^o} \delta A_{ij}^p \delta[t - t_{ij}^o - \delta t_{ij} - \Delta t_{ij}^p(d_q)] \\ + \frac{A_{ij}^{so}}{A_{ij}^o} \delta A_{ij}^s \delta[t - t_{ij}^o - \delta t_{ij} - \Delta t_{ij}^s(d_q)] \}, \end{aligned} \quad (5)$$

where $W_{ij}^p(t)$ and $W_{ij}^s(t)$ are the synthetic waveforms of depth phases corresponding to the direct phase described by $W_{ij}(t)$ (P , SV , or SH phase, numbered j on record i).

The set of inverted parameters is d_p , $S(t)$, M_0 , \mathbf{M} , δt_{ij} , t_{ij}^* , δA_{ij} , δA_{ij}^p , and δA_{ij}^s . However, because the inversion method is fully nonlinear, it is very flexible because it allows us to fix any of these parameters to an *a priori* value and to invert for the other ones. This flexibility is exploited in the [Inversion Strategies](#) section.

Data Selection and Normalization

The data used in this study are described in [Data and Resources](#). Broadband displacement records are obtained after deconvolution from instrument responses, band-pass filtering between 0.015 and 3 Hz, and rotation in the vertical, radial, and transverse coordinate system. For each record, different signal-to-noise ratio estimates are computed by comparing the energy inside the theoretical arrival-time window of the body wave with the one before the first arrival and before the body-wave arrival using L1 and L2 norms. We only keep records for which all these signal-to-noise ratio estimates are larger than 2.5.

To give equal weight to all records during the inversion process, amplitude variations due to radiation pattern and geometrical spreading are corrected by data normalization with respect to the amplitude of the body wave with maximum energy on the record. The normalization constant is defined by

$$A_i^R = \max_{1 < i < N_i} (A_{ij}^R), \quad (6)$$

where A_{ij}^R is the amplitude of the body-wave j measured on the record $\mathcal{R}_i(t)$, and N_i is the number of body waves taken into account on that record. The normalized records are defined by

$$\bar{\mathcal{R}}_i(t) = \frac{\mathcal{R}_i(t)}{A_i^R}. \quad (7)$$

A similar normalization is applied to the synthetics. In that case the normalization constant is defined by using synthetic amplitudes, including both source and propagation effects, and defined for each body wave by the following product:

$$A_{ij}^W = M_0 A_{ij}. \quad (8)$$

To be consistent, similar normalization is applied to synthetic seismograms:

$$A_i^W = \max_{1 < i < N_i} (A_{ij}^W). \quad (9)$$

The normalization factor of synthetic records changes during the inversion because it is strongly dependent on the moment tensor. Because source excitation can be very small for take-off angles close to nodal planes, a reference record with a high signal-to-noise ratio P wave far from nodal planes is chosen and referred to with the index i_o . The synthetic records are then normalized as

$$\bar{\mathcal{W}}_i(t) = \left(\frac{A_{i_o}^R A_i^W}{A_{i_o}^W A_i^R} \right) \frac{\mathcal{W}_i(t)}{A_i^W}. \quad (10)$$

The first term on the right side of equation (10) should be equal to one for perfect fit of the amplitudes, and the selection of record i_o ensures that $A_{i_o}^W$ cannot be close to zero.

This avoids problems of spurious amplification of the synthetics close to nodal planes.

The normalization of data and synthetics avoid the need to estimate the seismic moment (M_0). However, the seismic moment can be estimated for each body wave after the inversion of the rest of parameters from the following equation:

$$M_0 = \frac{A_{ij}^R}{A_{ij}}.$$

Inversion Method

In order to investigate high-frequency variations of the source time function, both displacement and velocity records are inverted simultaneously. The cost function (hereafter, called energy) is defined by

$$E(d_p, S(t), \mathbf{M}, \delta t_{ij}, \delta A_{ij}, \delta A_{ij}^p, \delta A_{ij}^s, t_{ij}^*) = \sum_i^{N_R} \|\bar{\mathcal{R}}_i(t) - \bar{\mathcal{W}}_i(t)\|_1 + \left\| \frac{d\bar{\mathcal{R}}_i}{dt}(t) - \frac{d\bar{\mathcal{W}}_i}{dt}(t) \right\|_1, \quad (11)$$

where N_R is the number of records, and $\|\cdot\|_1$ is the L1 norm (sum over all time points of absolute values of the function). We use an L1 norm because of its robustness relative to large differences between data and synthetics.

The inverse problem is solved with the simulated annealing approach (Kolář 2000; Chevrot, 2002; Garcia *et al.*, 2004; Garcia *et al.*, 2006; Tocheport *et al.*, 2007). The algorithm is extended here to the general case of all body waves and their depth phases. Simulated annealing is a variant of the Monte Carlo Markov Chain algorithms (Sen and Stoffa, 1995). It uses the analogy between the parameter space exploration and the annealing of a physical system for which thermodynamic theory predicts that the system reaches the lowest energy state if the cooling schedule is sufficiently slow. Temperature defines the probability of increasing the cost function (energy of the system) when one parameter is randomly perturbed. As the temperature decreases, the model space exploration is forced to focus on the lowest values of the cost function. The highest and lowest temperatures are chosen to impose, respectively, very high and very low probabilities of upward exploration of the cost function, whatever the number of waveforms and parameters. At the beginning of the cooling schedule, the memory of initial parameter values is lost quickly. Then, all the parameters converge to their optimal values at some critical temperature. The stability and computation time could be improved in future versions by refining the cooling schedule around the critical temperature of the system. However, in its present implementation, the convergence of the algorithm is ensured by a very low final temperature at the expense of computation time. Simulated annealing is chosen because it allows for handling of a large number of parameters (respectively, 1438 and 922 in the two examples presented in the following text). The resolution of each parameter is investigated empirically by performing three runs of the algorithm

with different random numbers. If the parameter converges to the same value for the three runs, it is assumed to be properly resolved. If the three estimates are dispersed, this parameter is not resolved correctly.

The STF $S(t)$ is approximated by the P wavelet, taken as a reference because attenuation is small for this particular phase. This makes the algorithm very efficient because we avoid recomputing the whole cost function each time we perturb a sample of the STF (Chevrot, 2002). Attenuation and/or Hilbert transforms, which are required to model other body waves from the reference P waveform, strongly decrease the efficiency of the algorithm because the convolutions by these operators need to be performed for each change of each point of the STF. During the simulated annealing cooling process, once the STF is recovered, amplitude and travel-time perturbations for each body wave quickly converge. Simulated annealing algorithms are difficult to optimize because of their intrinsic sequential character. However, the algorithm is partly parallelized by sending, when possible, independent computations on different processors through OpenMP (Dagum and Ramesh 1998). The two examples presented in the following text required 4 and 2 hours computation time, respectively, when inverting all the parameters on two quad-core Nehalem EX processors at 2.8 Ghz.

Inversion Strategies

We use the flexibility of the nonlinear inversion method to compare the results obtained after inversion using two different parametrizations.

For the first method (method 1), the body-wave amplitude perturbations (δA_{ij} , δA_{ij}^p , δA_{ij}^s) are fixed to 1, and the rest of the parameters (d_p , $S(t)$, M_0 , \mathbf{M} , δt_{ij} , and t_{ij}^*) are inverted. However, because local site amplifications at the receiver and errors in the instrument response are not modeled, the synthetic body-wave amplitudes may differ significantly from the real ones. To remove the most obvious amplitude errors (mainly from instrument responses of temporary stations), body-wave data with amplitudes 40 times less or higher than predicted by ray theory from Global CMT radiation are removed before inversion by method 1.

For the second method (method 2), all the parameters, including the body-wave amplitude perturbations, are inverted. Then the seismic moment is estimated during a second inversion process using synthetic body-wave amplitudes (A_{ij}^{WV}), obtained after the simulated annealing inversion, as input data and minimizing a cost function defined by

$$J(M_0, \phi, \gamma, \lambda) = \sum_{i=1}^{N_r} \sum_{j=1}^{N_i} |A_{ij}^{WV} - A_{ij}^M(M_0, \phi, \gamma, \lambda)|, \quad (12)$$

where M_0 is the seismic moment, ϕ , γ , and λ are, respectively, the strike, dip, and rake of the fault; N_r is the number of records; N_i is the number of body waves on record i ; and $A_{ij}^M(M_0, \phi, \gamma, \lambda)$ are ray theoretical amplitudes. The inversion is performed by grid search over strike, dip, and rake with angular steps of 5° , 2° , 5° , respectively. The best value

of M_0 is found by the steepest descent algorithm for each focal mechanism tested. With such a cost function, the records with the largest amplitudes have a more important weight than the others, as is usually the case for moment tensor inversions. The events described in the Examples section show the two inversion strategies.

The choice of body waveforms to invert has a strong influence on the solution. In principle, the method is able to handle any ray theoretical body waves; however, we keep only teleseismic P , SV , and SH waves, including their depth phases, for epicentral distances larger than 30° . By doing so, we avoid late arrivals with smaller signal-to-noise ratio, thus ensuring the quality and robustness of our source solutions, even though the algorithm is able to resolve body waveform interferences at triplications (Garcia *et al.*, 2006). The inversion of body waves around PKP or upper mantle triplications is beyond the scope of the present study.

Limitations

The main limitations of our method due to the waveform modeling that is limited by ray theory and point-source approximation. Ray theory does not handle diffracted waves. In addition, the algorithm is not able to process body waves with complex reflexion or transmission coefficients that introduce phase shifts that are not multiples of $\pi/2$. The point-source approximation attains its validity limits for earthquakes of moment magnitude above ≈ 7.0 . At larger magnitudes, the P waveforms are affected by directivity effects; the hypocenter and centroid locations start to differ, whereas they are assumed to be identical under the point-source approximation. Our method can be used safely up to moment magnitude of 7.5 for P waves. For larger magnitudes, the travel-time perturbations are more sensitive to the centroid than to the hypocenter location due to full waveform fit. This problem is not serious as long as the time difference between the onset and the centroid remains constant for all the waveforms. Because of directivity effects, this time difference will depend on the azimuth at large moment magnitudes. For these events, specific methodologies should be used (Kikuchi and Kanamori, 1991).

Examples

We illustrate our inversion method on two Japanese earthquakes having deep and shallow source locations. Because of slightly different *a priori* selection of the data for the two methods, some records present in method 2 may not be selected for method 1.

Example 1: A Japanese Deep Event

We first consider the event that occurred on 11 November 2005 at 15:36:31 GMT close to Kyushu in Japan (30.008° N, 130.031° E). Global CMT estimates of moment magnitude and depth are 6.2 and 155 km, respectively.

Figure 1 shows the evolution of model parameters during the simulated annealing inversion for method 1. When

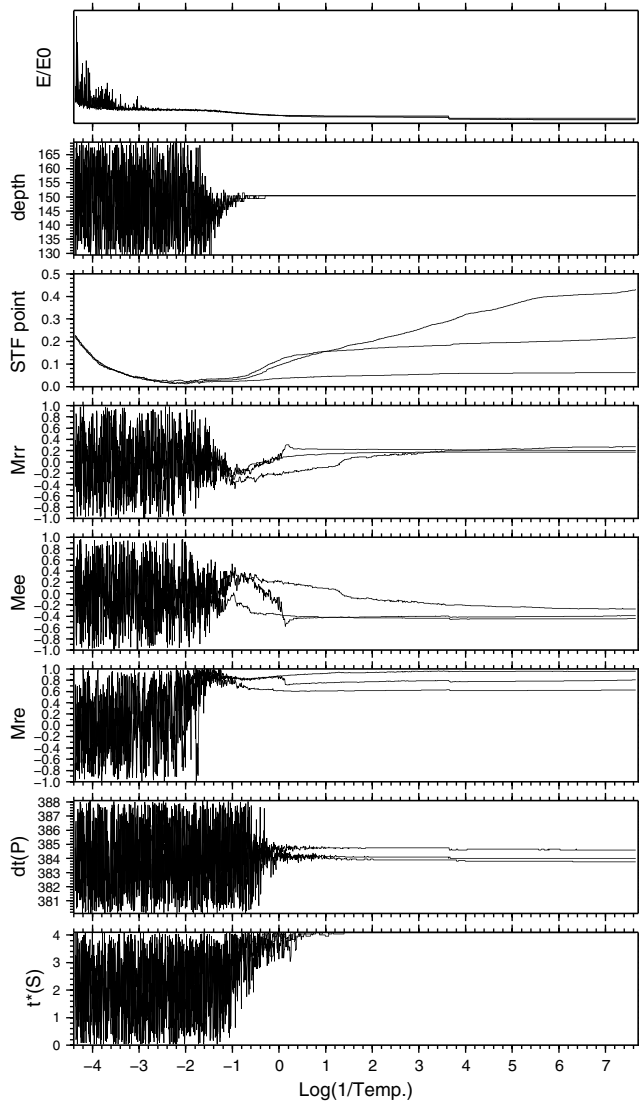


Figure 1. Evolution of various parameters during the inversion of the deep Japanese event as a function of the logarithm of the inverse of simulated annealing temperature. (top to bottom) Cost function scaled to its starting value, quake depth (in kilometers), $S(t_e)$ with $t_e = 4$ s, 3 components of the normalized moment tensor (M_{rr} , M_{ee} , and M_{re}), time shift ($t_{ij}^o + \delta t_{ij}$ in seconds) for a P wave, and attenuation parameter t_{ij}^* for an S wave. Three different runs of the simulated annealing inversion with different random number generator seeds are presented.

the temperature of the system cools down, the energy (or cost function) decreases, and the parameters converge to their final value. The simulated annealing is repeated three times in order to check that we obtain consistent results. The STF $S(t)$ is allowed to shift inside its window from one inversion to another. As a result, the plotted value of $S(t_e)$ (with $t_e = 4$ s) and the P -wave time shift vary between the three inversions, but the alignments of synthetic and data waveforms are almost identical. The source depth is the first parameter to converge and the best resolved (identical value for the three independent inversions). This is due to the waveform fit of depth phases that can be observed in

Figure 2d,e, respectively, about 40 and 55 seconds after P arrival for pP and sP phases. The attenuation parameter is the last to converge and the least well resolved, here saturating at its maximum value.

As observed in Figure 2, the two inversion methods give similar results. The source parameters are close to those of the Global CMT solution.

Example 2: A Japanese Shallow Event

We now consider a shallow event near the west coast of Honshu in Japan (37.339° N, 136.555° E), which occurred on 25 March 2007 at 00:41:57.8 GMT.

Figure 3 shows the evolution of model parameters during the simulated annealing inversion for the first method. As in the previous example, source depth is the first parameter to converge. All the parameters converged to similar values after the three runs of the simulated annealing procedure, which suggests that the final solution is robust. As illustrated in Figure 4, the Global CMT solution shows a significant non-double-couple component. We do not recover this component because we suppose our source solutions to be purely double couple. Nevertheless, in Figure 4b, the fit of P waveforms obtained with the first method is quite good, and the estimated depth of 10 km is close to the Global CMT solution which is 8 km. In particular, the waveforms are fitted by a positive P wave and a negative pP swing for azimuths larger than 180° . However, Figure 4c shows that the second inversion method does not reproduce correctly the polarity of some direct P waves close to the nodal plane, because synthetic direct P waveforms fit the pP waveforms that have a larger amplitude for azimuths around 270° . As a consequence, different depths are obtained for the three different simulated annealing inversions, which is an indication of inversion failure. This point illustrates the fact that adding a degree of freedom through the inversion of amplitude perturbation removes the constraint on the direct to depth phases relative amplitude ratio imposed by the radiation pattern. Once this constraint is removed, the depth phases can be fitted by the waveform of the direct phase or vice versa.

Application to Japan Earthquakes

We applied our inversion approach to a set of 143 Japanese events with magnitude larger than 5.7 in the time period 1990–2011. A map of these quakes is provided in Figure 5, and a complete list is provided in Table S1 in the electronic supplement to this article. This region is selected because we assume that the high density of regional networks may provide proper space/time locations and moment tensor estimates. In the time period 1997–2011, 85 of these events were located by the Japan Meteorological Agency (JMA). These locations, which rely on local and regional networks, are expected to be much more precise than the locations obtained by inverting teleseismic travel-time picks. In the same time period, the National Research Institute for Earth Science

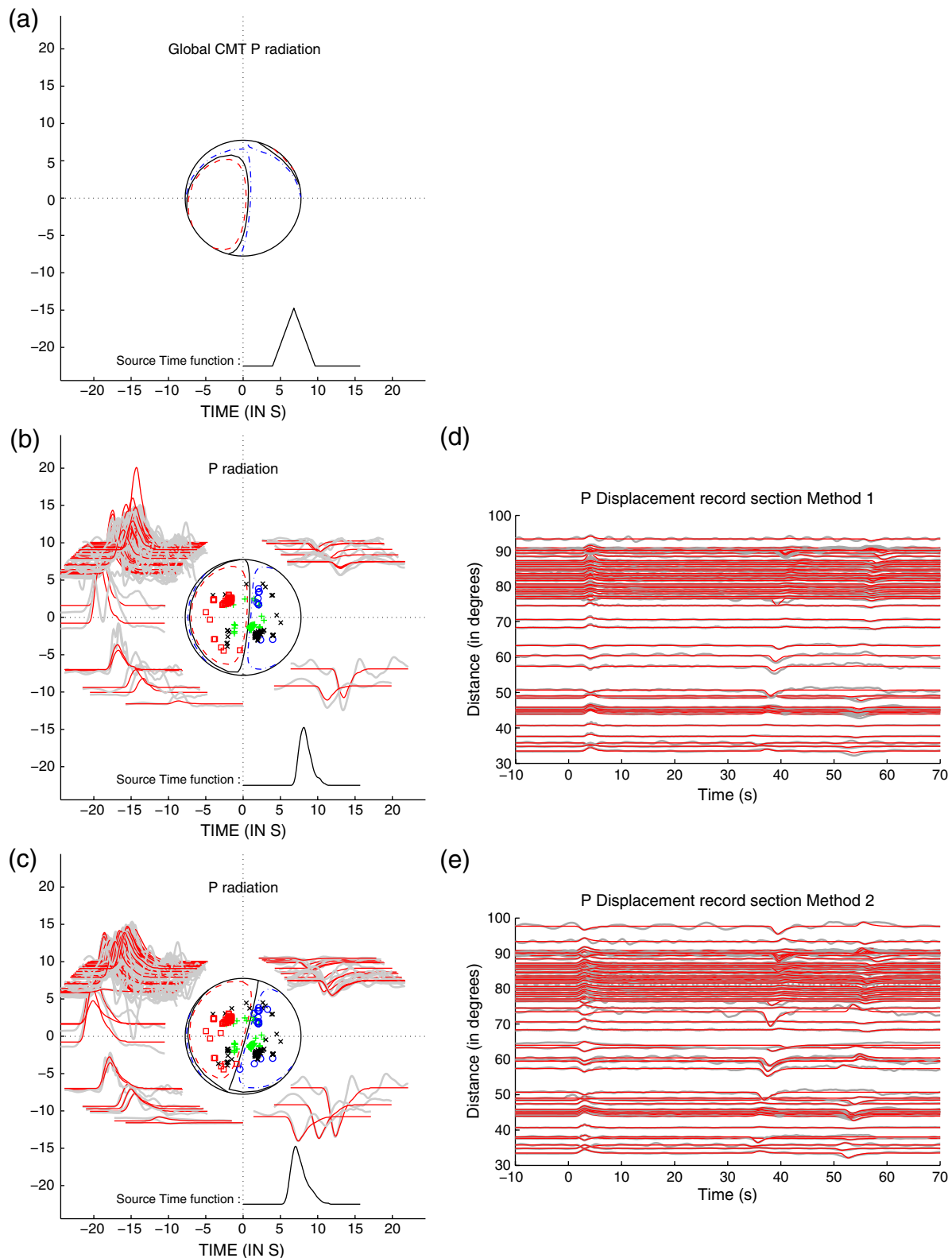


Figure 2. (a) Comparison of the Global CMT project solution, with the results of the (b and d) first and (c and e) second inversion methods for the deep event. Observed (thick lines) and synthetic (thin lines) seismograms are plotted around the focal sphere at positions corresponding to their azimuths, and normalized by their theoretical source radiation. Source time functions (at the bottom) are also given. Departure points are plotted on the focal sphere for P (squares and open circles), pP (crosses), and sP (plus symbols). Dashed and dot-dashed lines in the beach ball mark departure points of P waves with 10% amplitudes relative to their maximum value, respectively, for positive and negative first movements. Seismograms aligned on P wave arrival, and ordered by epicentral distance (in degrees) for the (d) first and (e) second inversion methods are also shown. The color version of this figure is available only in the electronic edition.

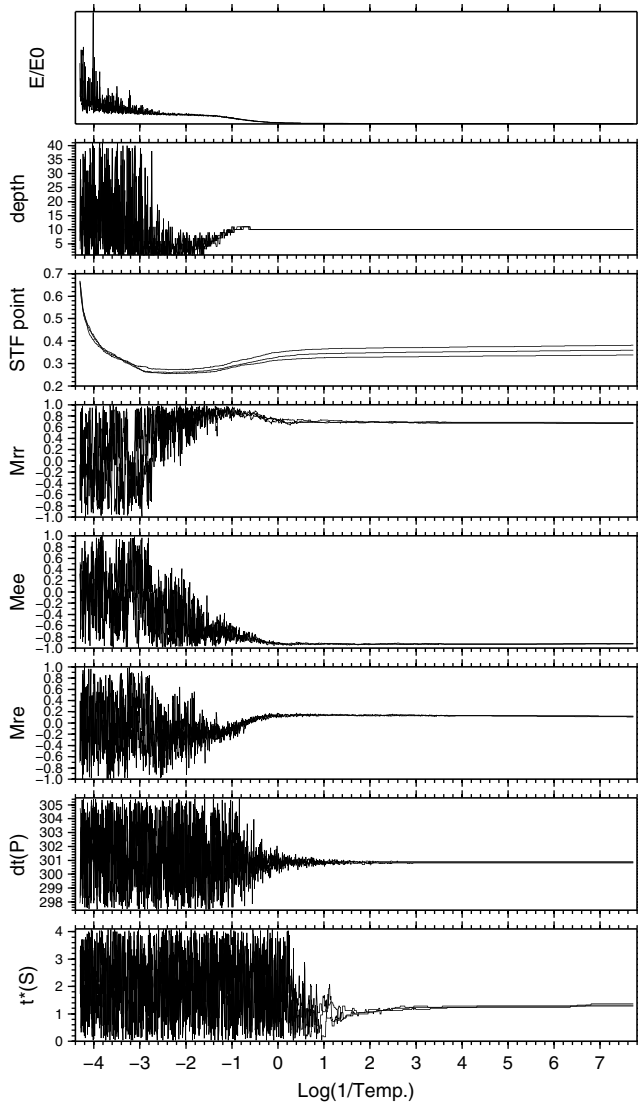


Figure 3. Evolution of various parameters during the inversion of one shallow event as a function of the logarithm of the inverse of simulated annealing temperature. (top to bottom) Cost function scaled to its starting value, event depth (in kilometers), $S(t_e)$ with $t_e = 4$ s, 3 components of the normalized moment tensor (M_{rr} , M_{ee} , and M_{re}), time shift ($t_{ij}^e + \delta t_{ij}$ in seconds) for a P wave, and attenuation parameter t_{ij}^* for a S wave. Three different runs of the simulated annealing inversion with different random number generator seeds are presented.

and Disaster Prevention (NIED) provided moment tensor estimates obtained by full waveform inversion of local broadband stations. These centroid moment tensor estimates are expected to be more precise than similar estimates obtained from teleseismic data (Kubo, 2002). We thus consider JMA locations and NIED moment tensor estimates as ground truth to evaluate the quality of our results.

Inverted model parameters are compared with those obtained by the Global CMT project (denoted CMT) (Dziewonski *et al.*, 1981), the National Research Institute for Earth Science and Disaster Prevention (denoted NIED) (Dreger and Helmberger, 1993; Kubo, 2002), the Japan Meteorologi-

cal Agency (denoted JMA), the United States Geological Survey (denoted USGS) (Sipkin, 1982, 1994), and EHB/ISC relocations and travel-time picks (Engdahl *et al.*, 1998; Bondár and McLaughlin, 2009). These comparisons between our results and other estimates are detailed in the following sections. Because we are using only teleseismic data, no Japanese record is used.

Source Time Function

The source time functions obtained with our approach are expected to contain more high-frequency information than the triangular function given by the Global CMT project. To quantify this improvement, we compute correlation coefficients between synthetics and observed seismograms. To do so, synthetic Green's functions are computed from the ak135 reference model (Kennett *et al.*, 1995) with the GEMINI software (Friederich and Dalkolmo, 1995) and convolved with the two different source time functions. The improvement in waveform fit is estimated by comparing the correlation coefficients between broadband data and P -wave synthetics using both our source time functions and the triangle functions in the Global CMT solutions. The body-wave records are selected by imposing similar travel-time residuals for the two estimates (absolute difference smaller than 0.4 s), average residuals smaller than 5 s, and average correlation coefficient larger than 0.9. The histogram of correlation coefficient differences is presented in Figure 6a. This histogram is shifted toward positive values, indicating that the correlation coefficients obtained using our source time functions are better than those using the simple triangular functions. This suggests that body-wave travel-time residuals measured by cross-correlation methods can be improved by using our refined source time functions.

The duration of an STF $S(t)$ is estimated from the window containing 98% of its energy (Vidale and Houston, 1993; Houston and Vidale, 1994; Tocheport *et al.*, 2007). An example is shown in Figure 6b. We compare our STF durations with those of the Global CMT project, which follows the scaling relation $L_{\text{CMT}} = 2.10 \left(\frac{M_0}{M_0^{\text{ref}}} \right)^{\frac{1}{3}}$ with $M_0^{\text{ref}} = 10^{17}$ Nm (Dziewonski *et al.*, 1981). Because our STF estimates are based on P waves and not corrected for P -wave attenuation, we expect our functions to be a low-pass version of the real source time functions. However, we have estimated this effect by synthetic tests assuming $t^* = 0.8$ s for shallow events and $t^* = 0.65$ s for deep events (Hwang and Ritsema, 2011). This effect is negligible for STF durations longer than 14 s and remains smaller than 1.5 s for shallow-event STF durations longer than 7.5 s and for deep-event STF durations longer than 5 s. Figure 7 shows the relation between the STF duration and seismic moment for Japanese earthquakes. As already noted by various authors, the STF duration of deep events is shorter than the one of shallow earthquakes (Tocheport *et al.*, 2007; Oth *et al.*, 2010); this difference cannot be explained by a difference of P -wave

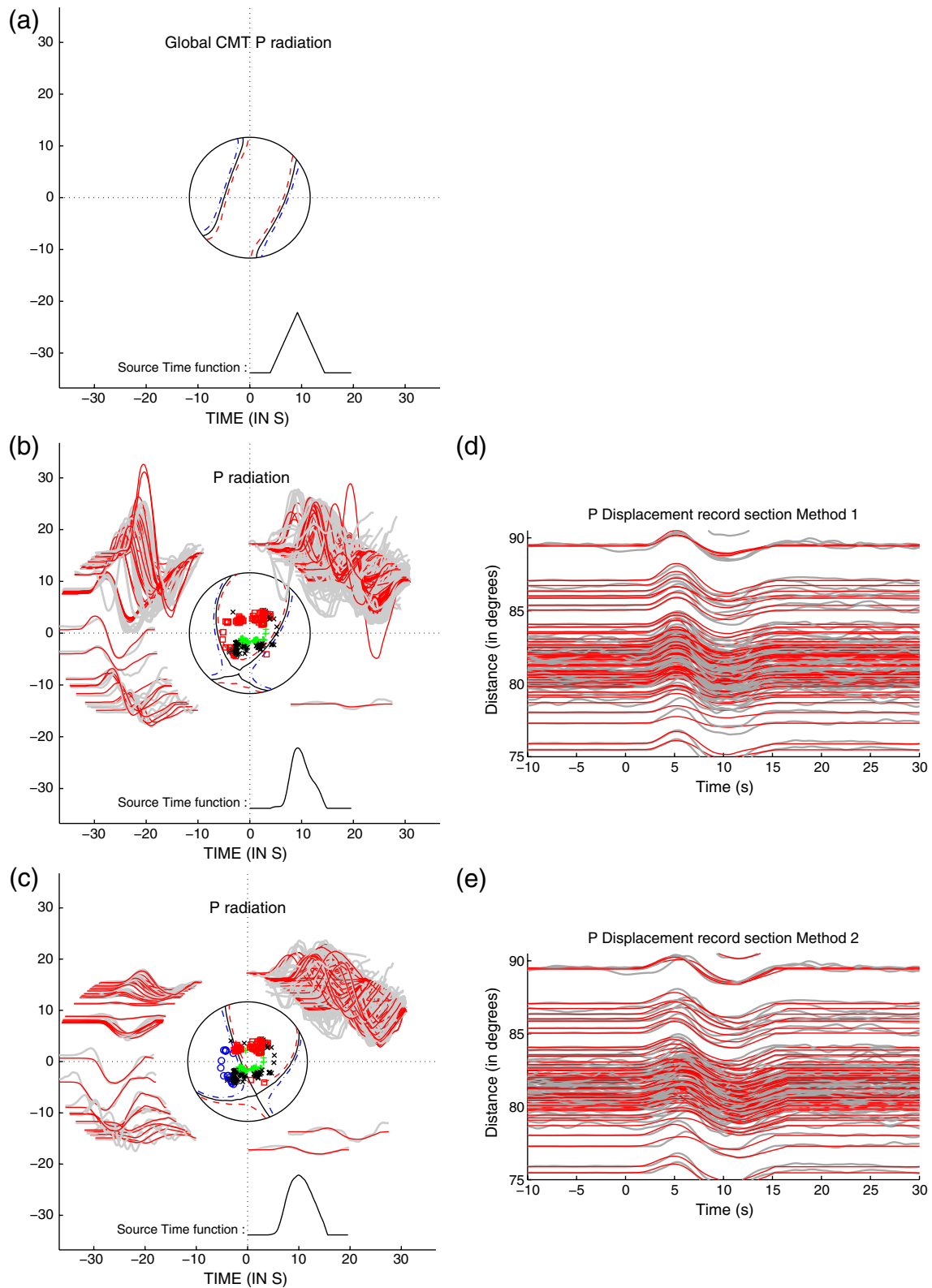


Figure 4. (a) Comparison of the Global CMT project solution, with the results of the (b and d) first and (c and e) second inversion methods for the deep event. Observed (thick lines) and synthetic (thin lines) seismograms are plotted around the focal sphere at positions corresponding to their azimuths, and normalized by their theoretical source radiation. Source time functions (at the bottom) are also given. Departure points are plotted on the focal sphere for P (squares and open circles), pP (crosses) and sP (plus symbols). Dashed and dot-dashed lines in the beach ball mark departure points of P waves with 10% amplitudes relative to their maximum value for positive and negative first movements, respectively. Seismograms aligned on P -wave arrival, and ordered by epicentral distance (in degrees) for the (d) first and (e) second inversion methods are also shown. The color version of this figure is available only in the electronic edition.

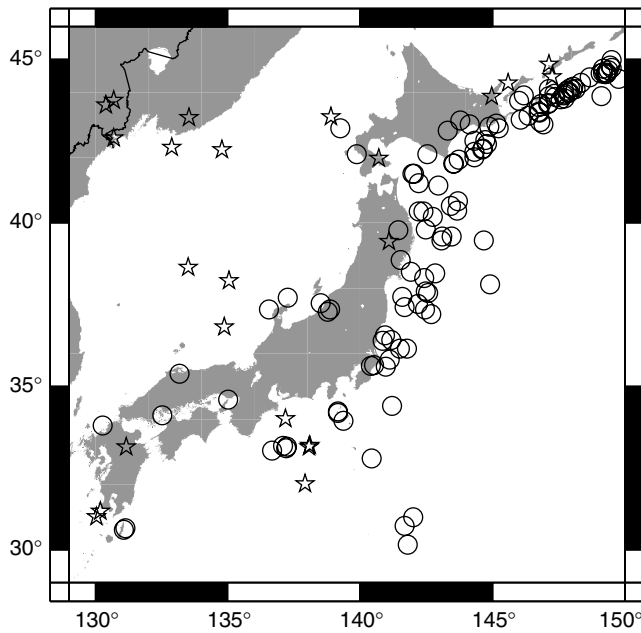


Figure 5. Position of earthquakes in the Japanese subduction area. Events deeper (shallower) than 110 km are indicated with a star (circle).

attenuation that induces an apparent STF duration difference smaller than 0.7 s. The deep/shallow STF duration difference is particularly significant for the largest earthquakes. A linear fit is presented, limited to seismic moments larger than $10^{18.3}$ Nm in order to avoid the P -wave attenuation effect at short STF durations. Because of the small data set and uncorrected attenuation effects, the error bars on the slopes are at least 0.05 and 0.1 for shallow and deep events, respectively. In Figure 7c, a slope of 0.295 ± 0.05 is observed for shallow events, which is close to the expected 0.33 scaling (Kanamori and Anderson, 1975), as already observed in the

same region (Oth *et al.*, 2010), or at smaller magnitudes in other regions (Abercrombie, 1995; Mayeda and Walter, 1996). Figure 7d shows that, when STF duration is multiplied by the shear-wave speed at the earthquake depth, the scaling is similar for deep and shallow events with slopes of 0.213 ± 0.1 and 0.297 ± 0.05 , respectively. This kind of scaling relation may provide a way to properly estimate the STF duration from seismic moment for both deep and shallow earthquakes, if it is validated on a global scale by future studies.

Source Depth

The source depth is always the first parameter to converge during the simulated annealing inversion, and probably the best resolved, because it is acting directly on the differential time between direct and depth phases. For events very close to the surface (depth < 15 km), this parameter may not be well resolved, because the waveforms of depth phases are sometimes incorporated into the STF estimate during its inversion. However, such problems are quite rare and easily detected by visual inspection. Methods of event source locations based on waveform inversion of surface waves are known to have difficulty in estimating properly the depth of shallow events due to trade-off between source depth and some components of the moment tensor (Ekström and Dziewonski, 1985). For this reason, we compare our depth estimates only with those obtained by other methods that exploited body-wave records. Results are presented in Table 1 and Figure 8. The average values are different because Japanese institutions (JMA and NIED) use a different velocity model for their locations. However, the difference between our depth estimates and JMA ones show standard deviations similar to EHB estimates, and smaller than USGS hypocenter estimates. NIED centroid depth statistics are also given for comparison. Both inversion methods give similar results

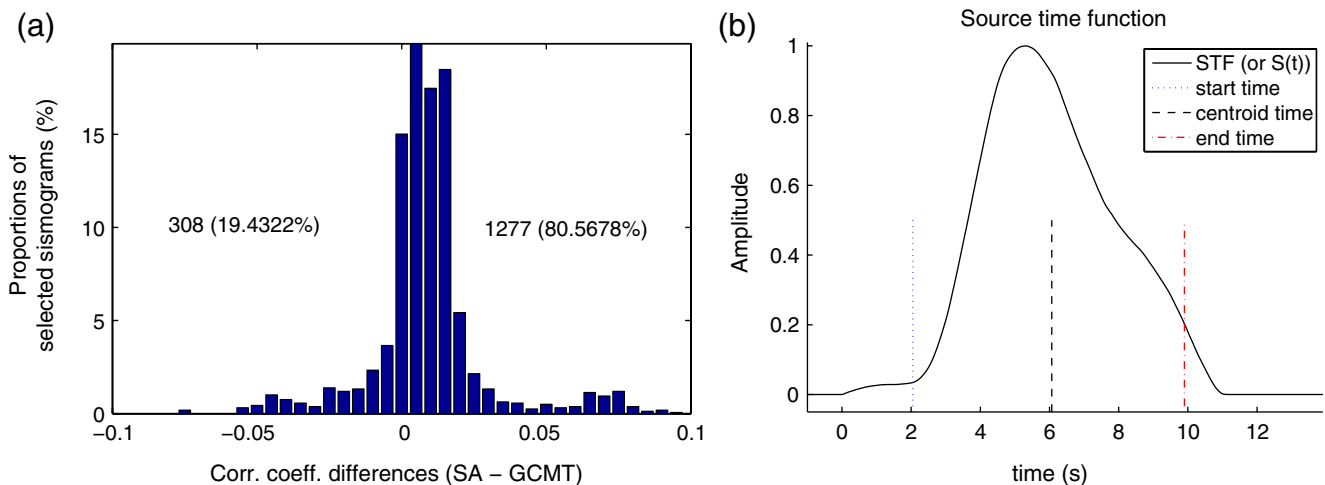


Figure 6. (a) Histogram of P -wave synthetic/data correlation coefficient difference by using our broadband source time function estimates and Global CMT ones. Positive values indicate a better correlation coefficient using our source time function estimates. Numbers and percentages indicate the number and percentages of P waveforms on both sides of zero, respectively. (b) Example of source time function duration determination for the shallow event inverted by method 1. The color version of this figure is available only in the electronic edition.

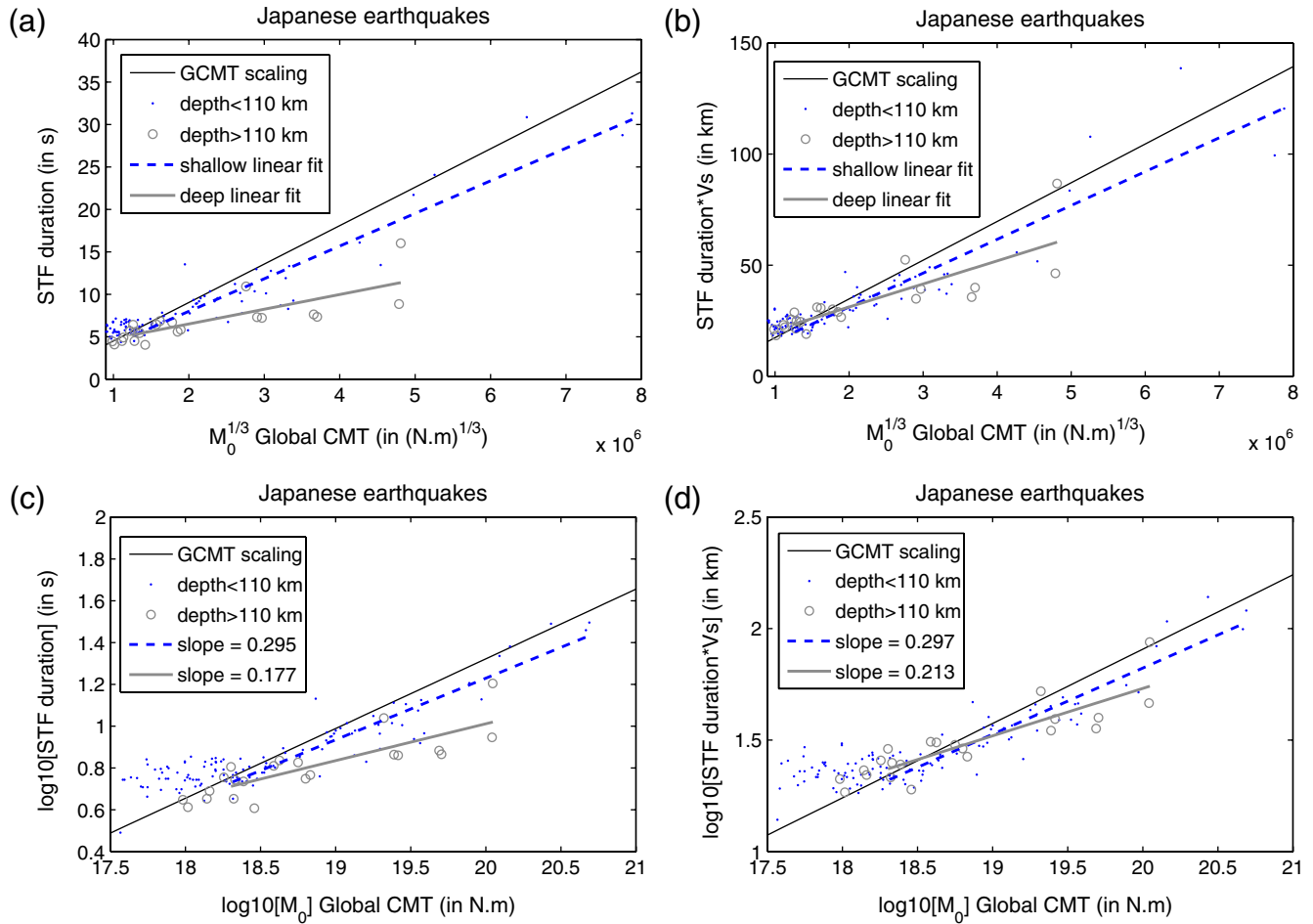


Figure 7. (a, b) STF duration (in seconds) and STF duration multiplied shear-wave velocity (in kilometers), as a proxy source dimension, as a function of $M_0^{1/3}$ and (c, d) as a function of $\log_{10}[M_0]$. Shallow events (depth < 110 km) and deep events (depth > 110 km) are indicated by dots and open circles, respectively. Linear fit is plotted for shallow events and deep events as a thick dashed line and a thick line, respectively. The thin line represents the Global CMT scaling relation, assuming a shear-wave crustal velocity of 3.85 km/s for panels (c) and (d). The color version of this figure is available only in the electronic edition.

because depth is properly resolved in both cases by the waveform fit of depth phases.

Seismic Moment and Moment Tensor

Seismic moment (M_0) and seismic moment tensor parameters must be inverted simultaneously because uneven coverage of the focal sphere introduces correlations between these parameters. Comparisons between our moment tensors and those of the NIED are shown in Figure 9 and Table 2. The same comparison is also shown with the Global CMT, USGS, and JMA solutions. Compared with NIED, the standard deviations of our moment magnitudes are similar to those of the USGS. However, the seismic moment estimates obtained with the first method are slightly shifted toward lower values, because of the equal weight given to all records whatever their absolute amplitude. By imposing this equal weight, lower amplitude records close to nodal planes have the same weight as large amplitude records. Because of the seismic energy traveling outside of the great circle path, seismic sta-

tions close to nodal planes generally have amplitudes larger than what is theoretically predicted. Consequently, the inversion will favor smaller seismic moments in order to fit these records. An improvement in this normalization issue would be to weight the records relative to their signal-to-noise ratio, even if in this case the normalization would be very similar to the usual absolute amplitude inversion.

Comparisons with seismic moment tensors provided by the NIED are performed with histogram plots of angular differences between P and T axis of our solutions with the NIED ones (Fig. 9). Both inversion methods provide broader histograms compared with other solutions. We ascribe this broadening to the influence of high-frequency unmodeled amplitude perturbations (wrong instrument response, site effects, and other influences) on the inverted data that are not present in the lower frequency data inverted by the other institutions. Moreover, we note in Figure 9c that the peak of the histogram distribution for the first inversion method is not centered on zero. This suggests that the different weights given to the data, compared with the usual scaling by absolute

Table 1
Statistics of Depth Estimate Comparison with JMA Hypocenter Depth Estimate*

Estimation Method	Whole Mean	Data Set Standard Deviation	Shallow Mean	Events (< 160 km) Standard Deviation
EHB hypocenter	-4.8	15.9	-3.6	13.5
Method 1	-6.7	15.3	-5.1	13.0
Method 2	-6.6	16.7	-4.0	13.5
USGS hypocenter	-14.3	24.5	-13.1	23.9
NIED centroid	-0.9	19.0	-3.3	14.3

*Mean and standard deviation of the difference between one data set and the JMA estimates are given in kilometers.

amplitude, produce a systematic shift of the solutions. The second inversion method shown in Figure 9d has a histogram peak closer to zero, indicating a smaller bias relative to the NIED solutions because the data weight is similar. However, some outliers traduce the remaining sensitivity of the second method to high-frequency amplitude deviations.

In conclusion, comparison with waveform inversion of low-frequency data (GCMT, USGS, NIED) shows that our results are quite sensitive to unmodeled amplitude perturbations at high frequency. This could be corrected empirically in future studies by computing station corrections for amplitudes that will include unmodeled effects such as instrument response and site effect. However, if it is desired to use the high-frequency amplitude perturbations for imaging, instrument responses should be better constrained to avoid biases.

Precise Differential Travel Times for Event Relocation

With our waveform inversion we obtain precise differential times between two stations for the same event because the same source time function is used to fit the two records. Method 1 provides better travel-time residual estimates than method 2, in particular for shallow events, because the cycle spiking observed on some records of Figure 4c is avoided by imposing relative amplitude constraints based on the seismic moment. To quantify travel-time measurement errors, we compute travel-time residuals and compare them with those

in the EHB/ISC catalog. We define a P single-difference residual between stations k and l for event i as

$$SD_i^{kl} = (td_i^k - td_i^l) - (to_i^k - to_i^l), \quad (13)$$

where td_i^k and to_i^k are, respectively, the observed and theoretical travel times of the P wave of event i at station k . We also define a P double-difference residual between stations k and l for events i and j as

$$DD_{ij}^{kl} = SD_i^{kl} - SD_j^{kl}. \quad (14)$$

The histograms of double-difference residuals obtained with method 1 (INV) and from EHB/ISC (EHB) are presented in Figure 10a for events close to each other in the Kuril Island region (latitude/longitude/depth ranges: 43° – 45° / 147.5° – 150° / 0 – 40 km). The variance of double-difference EHB residuals can be expressed as a sum of picking error variance (V_P) and event location error variance (V_L), because we can neglect the effect of Earth's lateral heterogeneities for events close to each other:

$$V_{DD}^{EHB} = 4V_P + 4V_L. \quad (15)$$

Similarly, the variance of double-difference residuals obtained with our method is given by the sum of single-difference measurement error variance (V_{SD}) and event location error variance (V_L):

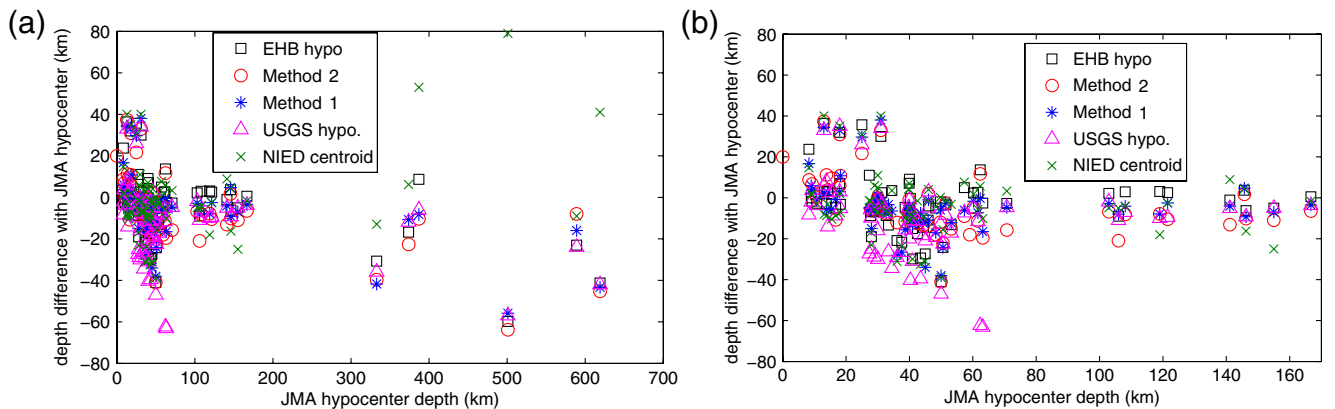


Figure 8. Comparison of depth estimates with estimates from Japan Meteorological Agency (JMA): (a) for the whole database, (b) zoom on shallow events. The color version of this figure is available only in the electronic edition.

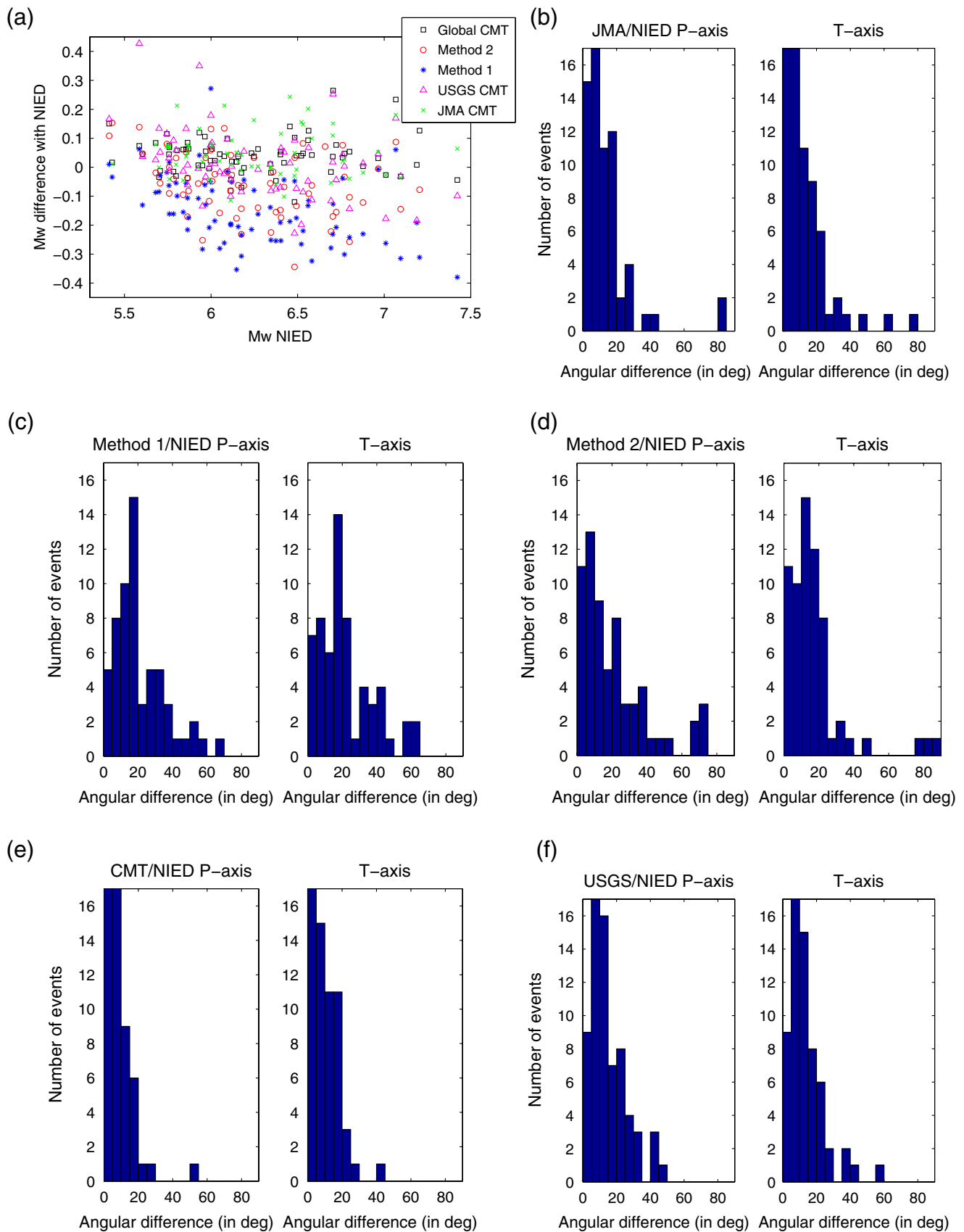


Figure 9. (a) Comparison of moment magnitude estimates with estimates from NIED. (b–f) histograms of P - and T -axis angular difference between NIED and other estimates. The color version of this figure is available only in the electronic edition.

Table 2
Statistics of Moment Magnitude and Radiation Pattern Difference with NIED
Estimates*

Estimation Method	Moment Mean	Magnitude Standard Deviation	P-Axis Standard Deviation (°)	T-Axis Standard Deviation (°)
Global CMT	0.040	0.063	12.0	11.9
Method 1	-0.147	0.120	25.7	25.9
Method 2	-0.056	0.110	28.7	24.5
USGS	-0.014	0.118	18.7	16.5
JMA	-0.004	0.247	20.0	19.0

*Mean and standard deviation are given for moment magnitude. Standard deviation of P - and T -axis angular difference are computed assuming symmetric histogram distribution around zero. This value has no real statistical meaning, but characterize the histogram dispersion around zero.

$$V_{DD}^{INV} = 2V_{SD} + 4V_L. \quad (16)$$

From the difference between equation (15) and (16), we estimate the difference $2V_P - V_{SD} = \frac{V_{DD}^{EHB} - V_{DD}^{INV}}{2}$ between two times for the picking error variance in the EHB/ISC data set and our single-difference measurement error variance. From Figure 10a, excluding differences larger than ± 4 s, $V_{DD}^{EHB} = 2.10 \pm 0.07 \text{ s}^2$ and $V_{DD}^{INV} = 1.36 \pm 0.04 \text{ s}^2$. Thus, $2V_P - V_{SD} \approx 0.4 \pm 0.1 \text{ s}^2$.

In order to estimate picking- and single-difference measurement errors independently, single differences for distances between stations smaller than 2° are extracted from the previous data set for events close to each other in the Kuril region. For such a data set, the effect of lateral heterogeneities is minimized because the distance between departure points or arrival points of the rays are smaller than 2° . In addition, the location errors are also minimized because for two stations close to each other, the location error for a given event is identical. Thus, the contribution of location error disappears in the single-difference variance. Neglecting the contribution of lateral heterogeneities and of event misloca-

tions, the single-difference variances computed for EHB/ISC residuals and for our data set are, respectively:

$$V_{SD}^{EHB} = 2V_P, \quad (17)$$

and

$$V_{SD}^{INV} = V_{SD}. \quad (18)$$

The histograms of the single differences for this data set are presented in Figure 10b. Because of strong restrictions on the interstation distances, the size of the data set is small (72 single differences), but it allows a rough estimate of picking- and single-difference measurement errors. We find $2V_P = 1.15 \pm 0.19 \text{ s}^2$ and $V_{SD} = 0.46 \pm 0.08 \text{ s}^2$. These estimates present large error bars due to the small size of the data set. However, they are consistent, within the error bar, with the values obtained from the analysis of double differences.

We thus estimate that the EHB/ISC picking error variance is $V_P \approx 0.5 \text{ s}^2$ and that the single-difference measurement error by our method is $V_{SD} \approx 0.5 \text{ s}^2$. The variance of double-difference residuals from EHB/ISC is about 2 s^2 , whereas it is about 1.0 s^2 with our method. This suggests

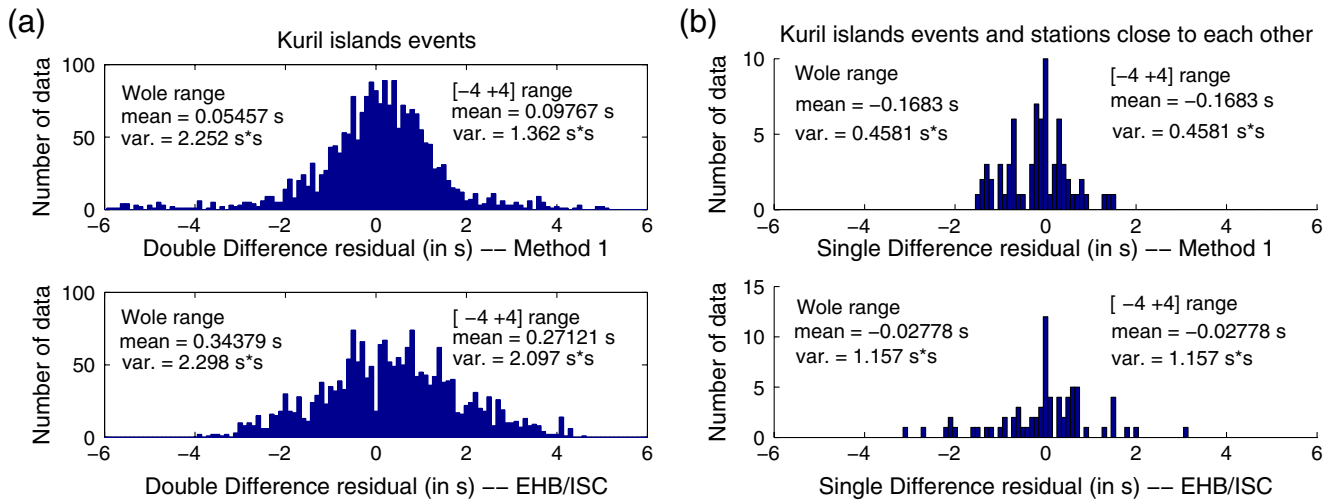


Figure 10. (a) Histograms of double-difference P -wave residuals from events in the Kuril islands region, obtained from method 1 (top) and from the EHB/ISC (bottom) for the same data set. (b) Histograms of single-difference P -wave residuals from events in the Kuril Islands region and interstation distances smaller than 2° , obtained from method 1 (top) and from the EHB/ISC (bottom) for the same data set. The color version of this figure is available only in the electronic edition.

that single- and double-difference residuals obtained with our method are more precise and may help to significantly improve event relocations relying on single- and double-difference algorithms.

S-Wave Attenuation

The attenuation parameter t_{ij}^* for shear waves is poorly resolved. However, we can determine its average as a function of distance using all the data of Japanese events. As shown in Figure 11, the average value of the attenuation parameter is around 2.5 s for propagation distances from 50° to 80° for both *SV* and *SH* waves. Because our source time function is a *P*-wave attenuated version of the real source time function, the real t^* value for the *S* wave should be the sum of the apparent t^* value and the t^* of *P* waves. Assuming an average t^* of 0.8 s for *P* waves, we obtain an average t^* value of 3.2 s for *S* waves, consistent with recent estimates (Hwang and Ritsema, 2011).

Discussion and Conclusions

The nonlinear inversion method of body waveforms described here is efficient and highly flexible because it allows us to choose the inverted parameters among a large set of source and body-wave parameters, or to properly fit the waveforms when different body waves interfere on the seismograms (direct and depth phases, or triplications). The flexibility of the method is exploited to infer two different inversion strategies related to different amplitude weighting of the records. It demonstrates that the relative weight of records strongly influences the recovery of the seismic moment tensor, and that imposing amplitude constraints based on the seismic moment allows a better recovery of travel times by reducing the risk of cycle skipping.

The retrieval of a high-frequency signal in the broadband source time function allows us to model observed waveforms more accurately, and consequently measure travel times by cross-correlation with more accuracy. The

duration of source time functions scales differently as a function of magnitude for shallow and deep earthquakes, but if shear-wave velocity is used as a proxy of rupture velocity, self similarity is observed. The event depth is the best resolved parameter and compares favorably with the EHB catalog. Moment magnitudes are consistent with other estimates within error bars and present standard deviations similar to those obtained by other body-waveform inversions, even if the first inversion method slightly underestimates the magnitudes. Moment tensor and attenuation parameters of shear waves are poorly resolved, owing to the difficulty to fit the high-frequency content of broadband waveforms. The strongest improvement is obtained for the determination of single-difference travel-time residuals that present standard deviations significantly lower than single pick estimates. We attribute this improvement to more accurate source time functions and event depths, and an optimal alignment of seismological records relying on waveform similarity instead of on travel-time picks on individual traces.

The method is limited by the ray theory and point-source approximations. It could be improved by optimizing the simulated annealing process, by applying crustal corrections and modifying the data-weighting scheme. The high-quality differential times will be used in future studies for precise event relocations. The broadband source time functions can also be used to improve deconvolution. This may have potential applications to receiver function studies. The broadband source time function can also be used to compute broadband synthetic seismograms, a crucial ingredient for future high-resolution imaging by full waveform inversion.

Data and Resources

All data used for this study were obtained at IRIS Data Management Center, and were collected by numerous seismic networks, which are listed here by their codes: AC, AD, AF, AG, AI, AK, AR, AT, AU, AV, AZ, BE, BI, BK, BL, BN, CB, CC, CH, CI, CN, CO, CU, CY, CZ, DK, DR, EM, EN,

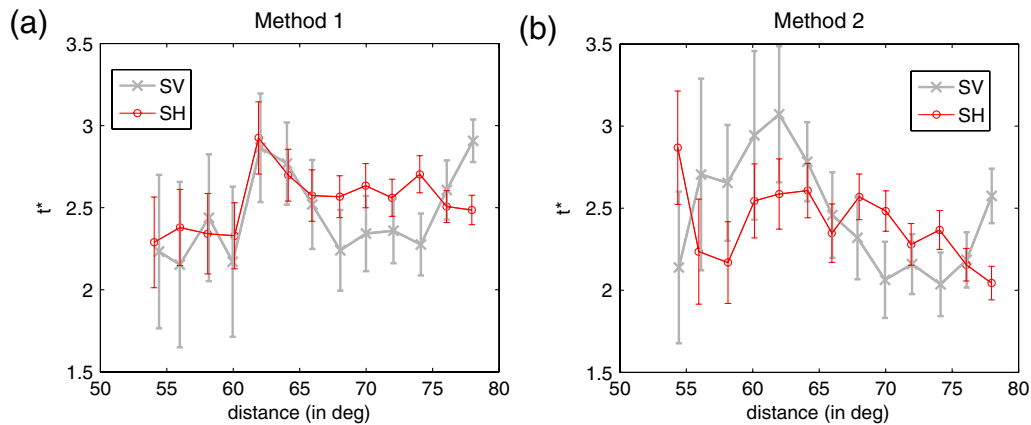


Figure 11. Average value of t_{ij}^* parameter of *SV* (crosses and thick line) and *SH* (open circles and thin line) waves by 2° distance bins computed by (a) the first inversion method and (b) the second inversion method. The color version of this figure is available only in the electronic edition.

EP, ER, ES, ET, FA, FR, G, GB, GD, GE, GL, GR, GS, GT, HK, HL, HT, HV, HW, IC, IE, II, IM, IP, IU, IW, JP, KN, KR, KZ, LB, LD, LI, LX, MB, MG, MI, MN, MR, MS, MX, MY, NA, ND, NE, NL, NM, NN, NO, NP, NR, NU, NV, NZ, OE, OV, PA, PB, PE, PI, PL, PM, PN, PO, PP, PR, PS, RE, RO, SB, SC, SF, SG, SS, SV, TA, TJ, TM, TR, TS, TT, TW, UK, UO, US, UU, UW, VE, WA, WY, and the various networks of the PASSCAL temporary experiment. We acknowledge these networks for providing their waveform data. The moment tensors and source parameters estimates were obtained from websites of the Global CMT project, the National Research Institute for Earth Science and Disaster Prevention, the Japan Meteorological Agency, and the United States Geological Survey. EHB/ISC relocations and travel-time picks were obtained from the website of the International Seismological Center. “ttimes” Fortran software and “CORAL” MATLAB toolbox were used in this study. The FORTRAN source code and documentation of the software presented here is available under “SAWIB” name (simulated waveform inversion of body waves) at <http://userpages.irap.omp.eu/~rgarcia> (last accessed September 2012). It will be available on software pages of the ORFEUS and IRIS institutions.

Acknowledgments

We acknowledge three anonymous reviewers and the Associate Editor for their detailed and helpful reviews. This work was performed using HPC resources from CALMIP (Grant 2012-P09101). This study was supported by INSU/CNRS through Programme National de Planétologie grants.

References

- Abercrombie, R. E. (1995). Earthquake source scaling relationships from -1 to $5 M_L$ using seismograms recorded at 2.5-km depth, *J. Geophys. Res.* **100**, 24,015–24,036, doi: [10.1029/95JB02397](https://doi.org/10.1029/95JB02397).
- Bondár, I., and K. McLaughlin (2009). Seismic location bias and uncertainty in the presence of correlated and non-Gaussian travel-time errors, *Bull. Seismol. Soc. Am.* **99**, 172–193, doi: [10.1785/0120080922](https://doi.org/10.1785/0120080922).
- Bondár, I., and D. Storchak (2011). Improved location procedures at the International Seismological Centre, *Geophys. J. Int.* **186**, 1220–1244, doi: [10.1111/j.1365-246X.2011.05107.x](https://doi.org/10.1111/j.1365-246X.2011.05107.x).
- Buland, R., and C. Chapman (1983). The computation of seismic travel times, *Bull. Seismol. Soc. Am.* **73**, 1271–1301.
- Červený, V. (2001). *Seismic Ray Theory*, Cambridge University Press, Cambridge, United Kingdom, 724 pp.
- Chevrot, S. (2002). Optimal measurement of relative and absolute delay times by simulated annealing, *Geophys. J. Int.* **151**, 164–171.
- Dagum, L., and R. Ramesh (1998). OpenMP: An industry standard API for shared memory programming, *IEEE Comput. Sci. Eng.* **5**, 46–55.
- Dreger, D. S., and D. V. Helmberger (1993). Determination of source parameters at regional distances with three-component sparse network data, *J. Geophys. Res.* **98**, 8107–8125, doi: [10.1029/93JB00023](https://doi.org/10.1029/93JB00023).
- Dziewonski, A., and J. Woodhouse (1983). An experiment in the systematic study of global seismicity: Centroid-moment tensor solutions for 201 moderate and large earthquakes of 1981, *J. Geophys. Res.* **88**, 3247–3271.
- Dziewonski, A., T.-A. Chou, and J. Woodhouse (1981). Determination of earthquake source parameters from waveform data for studies of global and regional seismicity, *J. Geophys. Res.* **86**, 2825–2852.
- Ekström, G., and A. Dziewonski (1985). Centroid-moment tensor solutions for 35 earthquakes in western North America (1977–1983), *Bull. Seismol. Soc. Am.* **75**, 23–39.
- Engdahl, E., R. Van der Hilst, and R. Buland (1998). Global teleseismic earthquake relocation with improved travel times and procedures for depth determination, *Bull. Seismol. Soc. Am.* **88**, 722–743.
- Friederich, W., and J. Dalkolmo (1995). Complete synthetic seismograms for a spherically symmetric Earth by a numerical computation of the Green’s function in the frequency domain, *Geophys. J. Int.* **122**, 537–550, doi: [10.1111/j.1365-246X.1995.tb07012.x](https://doi.org/10.1111/j.1365-246X.1995.tb07012.x).
- Garcia, R., S. Chevrot, and M. Weber (2004). Nonlinear waveform and delay time analysis of triplicated core phases, *J. Geophys. Res.* **109**, doi: [10.1029/2003JB002429](https://doi.org/10.1029/2003JB002429).
- Garcia, R., H. Tkalčić, and S. Chevrot (2006). A new global PKP data set to study Earth’s core and deep mantle, *Phys. Earth Planet. In.* **159**, 15–31, doi: [10.1016/j.pepi.2006.05.003](https://doi.org/10.1016/j.pepi.2006.05.003).
- Houston, H., and J. E. Vidale (1994). The temporal distribution of seismic radiation during deep earthquake rupture, *Science* **265**, 771–774, doi: [10.1126/science.265.5173.771](https://doi.org/10.1126/science.265.5173.771).
- Hwang, Y. K., and J. Ritsema (2011). Radial Q_μ structure of the lower mantle from teleseismic body-wave spectra, *Earth Planet. Sci. Lett.* **303**, 369–375, doi: [10.1016/j.epsl.2011.01.023](https://doi.org/10.1016/j.epsl.2011.01.023).
- Kanamori, H., and D. Anderson (1975). Theoretical basis of some empirical relations in seismology, *Bull. Seismol. Soc. Am.* **65**, 1073–1095.
- Kennett, B., E. Engdahl, and R. Buland (1995). Constraints on seismic velocities in the Earth from traveltimes, *Geophys. J. Int.* **122**, 108–124.
- Kikuchi, M., and H. Kanamori (1991). Inversion of complex body waves—III, *Bull. Seismol. Soc. Am.* **81**, 2335–2350.
- Kolář, P. (2000). Two attempts of study of seismic source from teleseismic data by simulated annealing non-linear inversion, *J. Seismol.* **4**, 197–213.
- Kubo, A., E. Fukuyama, H. Kawai, and K. Nonomura (2002). NIED seismic moment tensor catalogue for regional earthquakes around Japan: Quality test and application, *Tectonophysics* **356**, 23–48, doi: [10.1016/S0040-1951\(02\)00375-X](https://doi.org/10.1016/S0040-1951(02)00375-X).
- Mayeda, K., and W. R. Walter (1996). Moment, energy, stress drop, and source spectra of western United States earthquakes from regional coda envelopes, *J. Geophys. Res.* **101**, 11,195–11,208, doi: [10.1029/96JB00112](https://doi.org/10.1029/96JB00112).
- Oth, A., D. Bindi, S. Parolai, and D. Di Giacomo (2010). Earthquake scaling characteristics and the scale-(in)dependence of seismic energy-to-moment ratio: Insights from KiK-net data in Japan, *Geophys. Res. Lett.* **37**, L19304, doi: [10.1029/2010GL044572](https://doi.org/10.1029/2010GL044572).
- Röhms, A., J. Trampert, H. Paulssen, and R. Snieder (1999). Bias in reported seismic arrival times deduced from the ISC bulletin, *Geophys. J. Int.* **137**, 163–174.
- Ruff, L. J. (1989). Multi-trace deconvolution with unknown trace scale factors: Omnilinear inversion of P and S waves for source time functions, *Geophys. Res. Lett.* **16**, 1043–1046, doi: [10.1029/GL016i009p01043](https://doi.org/10.1029/GL016i009p01043).
- Sen, M., and P. Stoffa (1995). *Global Optimization Methods in Geophysical Inversion*, Elsevier, Amsterdam, The Netherlands, 281 pp.
- Sipkin, S. (1982). Estimation of earthquake source parameters by the inversion of waveform data: Synthetic waveforms, *Phys. Earth Planet. In.* **30**, 242–259.
- Sipkin, S. A. (1994). Rapid determination of global moment-tensor solutions, *Geophys. Res. Lett.* **21**, 1667–1670, doi: [10.1029/94GL01429](https://doi.org/10.1029/94GL01429).
- Tocheport, A., L. Rivera, and S. Chevrot (2007). A systematic study of source time functions and moment tensors of intermediate and deep earthquakes, *J. Geophys. Res.* **112**, B07311, doi: [10.1029/2006JB004534](https://doi.org/10.1029/2006JB004534).
- Vidale, J. E., and H. Houston (1993). The depth dependence of earthquake duration and implications for rupture mechanisms, *Nature* **365**, 45–47, doi: [10.1038/365045a0](https://doi.org/10.1038/365045a0).

Université de Toulouse; UPS-OMP; IRAP
Toulouse, France